Fabrication of high photocatalytic activity and easy recovery photocatalysts with ZnFe$_2$O$_4$ supported on ultrathin MoS$_2$ nanosheets

Wei Ma[1,3] · Na Wang[1] · Liuqing Yang[1] · Manfei Lv[1,2] · Zhi Zhu[4] · Songtian Li[1]

Abstract

Loading of ZnFe$_2$O$_4$ on ultrathin MoS$_2$ nanosheets were performed to enhance the photocatalytic activity and recovery property by a facile hydrothermal method. The ZnFe$_2$O$_4$/MoS$_2$ photocatalysts showed a relatively high photocatalytic activity than ZnFe$_2$O$_4$ and MoS$_2$ under visible light irradiation, and the degradation rate of tetracycline hydrochloride by the MoS$_2$/ZnFe$_2$O$_4$-25% photocatalysts is up to 95%. Systematical characterization demonstrated that the synergistic effect of nanosheets structure of MoS$_2$ and heterostructures formed by ZnFe$_2$O$_4$ and MoS$_2$ could effectively enhance light absorption ability, increase reactive sites, inhibit recombination of the photo-generated electrons and holes, accelerate the photo-generated electrons transfer speed, and improve photocatalytic performance of the photocatalysts. The ZnFe$_2$O$_4$/MoS$_2$ photocatalysts could be recovered quickly under the external magnetic field and reused four times with no significant decrease in photocatalytic activity. The ·O$_2^-$ is the main active species.

1 Introduction

Increasingly, severe environmental pollution is one of the urgent problems to be solved in the world. To solve the environmental pollution problems, many traditional technologies have been adopted, such as incineration, biological method, stripping method, and activated carbon adsorption method. However, these methods will produce secondary pollution, which is more harmful to the environment. Semiconductor photocatalytic technology, as a green environmental technology, with its high efficiency and environmental friendliness, has been widely used. Semiconductor photocatalyst can absorb and utilize solar energy more effectively and is an active ecological purification material [1–5]. The photocatalysts, such as mixed transition metal oxides, titanate, niobate, and tantalite, can only absorb ultraviolet light, but ultraviolet radiation accounts for only 4% of the incident solar energy. To improve the conversion efficiency of solar energy [6–8], the basic approach is to develop and design visible-light-driven photocatalysts.

Recently, researchers are increasingly interested in low-cost and high-efficiency photocatalysts; Zinc ferrite (ZnFe$_2$O$_4$) with the spinel crystal structure and narrow E_g (1.9 eV) is an important research direction of the photocatalysts. It has a wide range of functional characteristics in practical applications, such as magnetism, visible light response, and excellent photochemical stability [9–12]. However, single ZnFe$_2$O$_4$ is widely restricted and ascribed to the quick rejoining of photoexcited charge carriers and natural agglomeration, which is limiting its practical application. Therefore, it is significant to develop a method to improve charge separation and photocatalytic activities of ZnFe$_2$O$_4$.

Construction of heterojunctions is a feasible and straightforward way to enhance photocatalytic performance of single photocatalysts, and the modified composite photocatalysts have excellent electronic properties and effective separation of photo-generated electron and hole pairs [13, 14]. Molybdenum disulfide (MoS$_2$) is a graphene-type transition metal dichalcogenides compound with an ultrathin layered structure and a suitable energy bandgap [15, 16],

✉ Songtian Li
lisongtian@126.com

1   Henan Key Laboratory of Research for Central Plains Ancient Ceramics, School of Chemistry and Environmental Engineering, Pingdingshan University, Pingdingshan 467099, China

2   College of Chemistry and Molecular Engineering, Zhengzhou University, Zhengzhou 450000, China

3   Department of Chemistry, Tsinghua University, Beijing 100084, China

4   School of Chemistry and Chemical Engineering, Institute of the Green Chemistry and Chemical Technology, Jiangsu University, Zhenjiang 212013, China

which has significant potential applications in the field of nanoelectronics, optoelectronics, and flexible devices. Furthermore, MoS_2 has the advantages of low cost, near-zero *Gibbs* free energy, excellent rich edge structure, and large surface area [17–24] and has been widely used in the study of photocatalysis.. The strategy of integrating $ZnFe_2O_4$ with MoS_2 nanosheets was proposed, which can improve the light absorption ability of the composite photocatalysts because of the introduction of nanosheets structure of MoS_2. Meanwhile, magnetic separation can effectively prevent the loss of the catalysts in the recovery process, and it is more environmentally friendly to show broad application potential.

In the study, high photocatalytic activity and easy recovery photocatalysts such $MoS_2/ZnFe_2O_4$ heterostructure photocatalysts were synthesized by the hydrothermal method. The introduction of nanosheet structure of MoS_2 and heterostructures formed by $ZnFe_2O_4$ and MoS_2 can effectively improve light absorption ability, increase reactive sites, effectively inhibit recombination of the photo-generated electrons and holes, accelerate the photo-generated electrons transfer speed, and enhance photocatalytic performance of the photocatalysts.

2 Experimental

2.1 Material

$(NH_4)_6Mo_7O_{24}\cdot4H_2O$, thiourea, $Fe(NO_3)_3\cdot9H_2O$, $Zn(NO_3)_2\cdot6H_2O$, tartaric acid, and sodium hydroxide (NaOH) were purchased from Sinopharm Chemical Reagent Co., Ltd. All reagents were analytical grade and used without further purification in this research.

2.2 Preparation of MoS₂

MoS_2 were synthesized by the conventional hydrothermal method [25]. 0.8 g of $(NH_4)_6Mo_7O_{24}\cdot4H_2O$ and 6.4 g of thiourea were dissolved in 80 mL of deionized water and stirred for 1 h. The homogeneous solution was transferred into PTEF-lined autoclave and maintained at 200 °C for 24 h. Then, the samples were obtained by centrifugation, washed with deionized water and ethanol, and dried in a vacuum oven at 60 °C.

2.3　2.3. Preparation of ZnFe₂O₄ [10]

20 mmol $Fe(NO_3)_3\cdot9H_2O$ and 10 mmol $Zn(NO_3)_2\cdot6H_2O$ were dissolved in 30 mL of deionized water and stirred for 30 min. After that, 60 mmol tartaric acid was added to solutions mentioned above and stirred for 30 min, 220 mmol NaOH was added and stirred for 30 min, the mixture solution was transferred into PTEF-lined autoclave and maintained at 180 °C for 24 h. Then, the samples were obtained by magnetic separation method, washed with deionized water and ethanol, and dried in a vacuum oven at 60 °C.

2.4　Preparation of MoS₂/ZnFe₂O₄ photocatalysts

$MoS_2/ZnFe_2O_4$ photocatalysts were synthesized by a facile hydrothermal method. The prepared $ZnFe_2O_4$ of certain quality was sonicated thoroughly in 80 mL deionized water for 1 h. 0.8 g of $(NH_4)_6Mo_7O_{24}\cdot4H_2O$ and 6.4 g of thiourea were dissolved in 80 mL of deionized water and stirred for 1 h. The homogeneous solution was transferred into PTEF-lined autoclave and maintained at 200 °C for 24 h. Then, the samples were obtained by magnetic separation method, washed with deionized water and ethanol, and dried in a vacuum oven at 60 °C.

The quality of $ZnFe_2O_4$ added is controlled to be 1.44 g, 0.72 g, 0.29 g, and 0.144 g, and the obtained samples are accordingly marked as $MoS_2/ZnFe_2O_4$-5%, $MoS_2/ZnFe_2O_4$-10%, $MoS_2/ZnFe_2O_4$-25%, and $MoS_2/ZnFe_2O_4$-50%, respectively.

2.5　Instrumentation

The powder XRD patterns are collected on an X-ray diffractometer (SMART LAB, RIGAKU, Japan) with the scanning range of $2\theta = 10°$–70°. The scanning electron microscope (SEM) images were examined with S-8010 (HITACHI, Japan). The transmission electron microscope (TEM) micrographs were taken with an HT-7700 (HITACHI, Japan) operated at 100 kV. The surface chemical compositions were investigated by X-ray photoelectron spectroscopy (XPS) with an Omicron ESCALAB 250Xi (Thermo Fisher) probe spectrometer. Fourier transform-infrared (FT-IR) spectra were tested by Nicolet Model Nexus 470 FT-IR (Thermo Fisher, American). The UV–visible diffuse reflectance spectrum (UV–vis DRS) was recorded in a UV-3600 spectrophotometer (Shimadzu, Japan) and $BaSO_4$ to test all the samples for reference. Photoluminescence (PL) spectra were obtained on F-7000 (Hitachi, Japan) fluorescence spectrophotometer. Measurement of the magnetic property of the prepared photocatalysts was tested by using a vibrating sample magnetometer (VSM, HH-15, China). The visible light irradiation was obtained from a 300 W xenon lamp (CEL-HXF300, Beijing China Education Au-light Co. Ltd., China) with a 420 nm cutoff filter. Electron spin resonance (ESR) was tested on an electron paramagnetic resonance spectrometer (A300-10/12, Bruker).

The electrochemical and photoelectrochemical properties were tested on an electrochemical system (CHI-660B, China). The photoelectric responses of the obtained photocatalysts were measured at 0.0 V with ITO as a working

electrode, a platinum wire as a counter electrode, and a standard calomel electrode (SCE) as a reference electrode.

2.6 Photocatalytic activity experiments

The study evaluated the photocatalytic activity of MoS_2, $ZnFe_2O_4$, and $MoS_2/ZnFe_2O_4$ prepared in advance by degradation TC under visible light irradiation. 100 mg photocatalysts were added into $100\,mL \times 10\,mg\,L^{-1}$ TC solution. Firstly, the study used ultrasonication to disperse the photocatalysts for 10 min, and after stirring for 2 h in the dark, the dynamic adsorption equilibrium was achieved between TC and photocatalysts. The solution after the reaction was extracted in a specified interval of time. TC concentration was measured by UV–vis spectroscopy at 275 nm, and the change in concentration was recorded as C/C_0 (where C_0 was the initial TC concentration, C was the concentration of time t). Other conditions remain unchanged, and TC were directly photolyzed without the photocatalysts in the reaction system.

3 Result and discussion

3.1 Material characterization

The XRD patterns of prepared MoS_2, $ZnFe_2O_4$, and $MoS_2/ZnFe_2O_4$ photocatalyst were shown in Fig. 1. In the figure, for the spectrum of MoS_2, only four broad XRD peaks at $2\theta = 14°$, 33.3°, 39.6°, and 58.5° were found, respectively, indexing to the (002), (101), (103), and (110) crystal plane of MoS_2 (JCPDS card No. 37-1492) [25], which revealed the formation of MoS_2 in hydrothermal process. As shown in the figure, the original $ZnFe_2O_4$ shows (220), (311), (400), (422), (511), and (440) diffraction peaks on the crystal plane
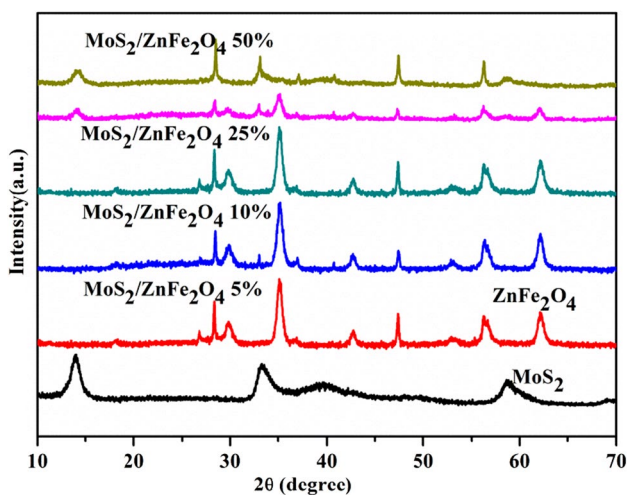
at 2θ values of 30.0°, 35.3°, 43.0°, 53.2°, 56.7°, and 62.2°, respectively, which were indexed to spinel-type $ZnFe_2O_4$ (JCPDS card No. 22-1012) [26]. $MoS_2/ZnFe_2O_4$ photocatalysts show similar diffraction peaks to those of the original $ZnFe_2O_4$. The XRD patterns of the $ZnFe_2O_4$ did not change, while the loading amount of MoS_2 increased from 5 to 50%, the diffraction peaks of MoS_2 only exist in $MoS_2/ZnFe_2O_4$-25% and $MoS_2/ZnFe_2O_4$-50% photocatalysts, and no significant signal of MoS_2 was discovered from the spectra of other $MoS_2/ZnFe_2O_4$ photocatalysts, probably due to its low loading amount and high dispersion of MoS_2 in the $MoS_2/ZnFe_2O_4$ photocatalysts.

The FT-IR spectra of pure MoS_2, $ZnFe_2O_4$, and $MoS_2/ZnFe_2O_4$ photocatalysts are seen in Fig. 2. Two main broad peaks in 900 and 450 cm^{-1} were ascribed to metal–oxygen (M–O), determiing the existence of spinel ferrite [27]. The maximum value seen between 600 and 500 cm^{-1} corresponds to the stretching vibration of the primary metal at A-site, $M_{tetra} \leftrightarrow O$, in comparison the minimum peak showed from 450 to 400 cm^{-1} ascribed to the stretching vibration of B-site metal, $M_{octa} \leftrightarrow O$. The MoS_2 had two characteristic peaks at 1100 and 620 cm^{-1} in the FT-IR spectrum and the intensity of the two unique peaks of MoS_2 weakened in the $MoS_2/ZnFe_2O_4$ photocatalysts.

The study determined the light absorption capacity of the photocatalysts by UV–vis DRS. Figure 3a displays the UV–vis DRS of the MoS_2, $ZnFe_2O_4$, and $MoS_2/ZnFe_2O_4$ photocatalysts. The MoS_2 and $MoS_2/ZnFe_2O_4$ photocatalysts exhibit higher light-absorbing property than $ZnFe_2O_4$ at wavelength from 600 to 800 nm, and the spectra of $MoS_2/ZnFe_2O_4$ 25% showed a slight red shift, since MoS_2 as a thin layer structure was uniformly deposited on $ZnFe_2O_4$ to make the light transmit evenly, which is conducive to improving
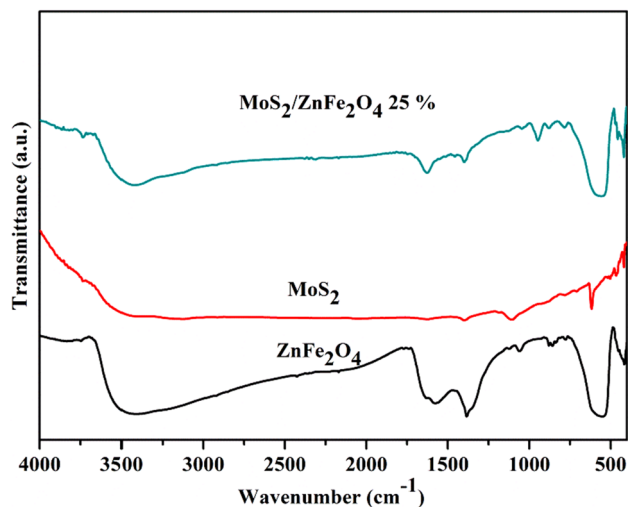

Fig. 1 XRD patterns of the pure MoS_2, $ZnFe_2O_4$, and $MoS_2/ZnFe_2O_4$ photocatalysts

Fig. 2 FT-IR spectra of the pure MoS_2, $ZnFe_2O_4$, and $MoS_2/ZnFe_2O_4$ 25% photocatalysts
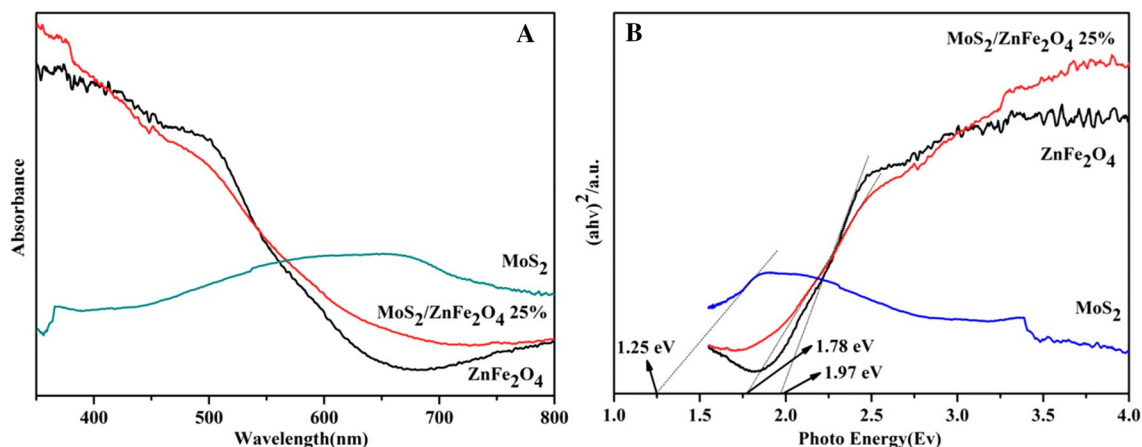
Fig. 3 UV–vis DRS (**a**) and estimation of bandgap energy (**b**) of MoS_2, $ZnFe_2O_4$, and $MoS_2/ZnFe_2O_4$ 25% photocatalysts

the light absorption of the photocatalysts. Figure 3b is the correlation curve of $(\alpha h\nu)^2$ versus $h\nu$ to obtain the bandgap of the MoS_2, $ZnFe_2O_4$, and $MoS_2/ZnFe_2O_4$ photocatalysts. In line with *Kubelka–Munk* formula, the bandgap (E_g) of the MoS_2, $MoS_2/ZnFe_2O_4$ 25%, and $ZnFe_2O_4$ photocatalysts were calculated to be 1.25 eV, 1.78 eV, and 1.97 eV, respectively. The electrons on the valence band (VB) are more easily excited for the smaller bandgap photocatalysts under visible light and jump to the conduction band (CB), which is conducive to the photocatalytic response. Consequently, $MoS_2/ZnFe_2O_4$ photocatalysts can effectively utilize visible light and participate in photocatalytic reaction.

The composition of $MoS_2/ZnFe_2O_4$ and the chemical states of different elements were determined by XPS. As can be seen in Fig. 4, in line with the XPS observations, Mo, S, Zn, Fe, and O elements are detected in the $MoS_2/ZnFe_2O_4$ photocatalysts (Fig. 4a). The high-resolution Mo 3d XPS spectrum (Fig. 4b) shows the binding energies peaks of Mo $3d_{5/2}$ and Mo $3d_{3/2}$ at 229.0 and 232.1 eV, respectively, which are assigned to Mo^{4+} in MoS_2 [28–30]. The S 2p XPS spectrum (Fig. 4c) determines the existence of both monosulfide S^{2-} (S $2p_{3/2}$ and S $2p_{1/2}$ at 161.7 and 162.8 eV, respectively), which are consistent with the previous literature reports on MoS_2 [15, 28, 29]. The symmetric peaks at 1021.3 eV and 1044.4 eV are ascribed to Zn $2p_{3/2}$ and Zn $2p_{1/2}$, respectively (Fig. 4d), and the peaks at 712.7 eV and 725.4 eV are indexed to Fe $2p_{3/2}$ and Fe $2p_{1/2}$ (Fig. 4e) [1]. Furthermore, the peaks at 531.1 eV and 529.7 eV can belong to the binding energy of O 1s (Fig. 4f).

The morphology and size of the photocatalysts were studied by SEM. In Fig. 5a, the SEM image of MoS_2 reveals that the MoS_2 microspheres were composed of nanosheet with the dimension in the range of 300–400 nm assembled by densely packed petals. In Fig. 5b, it can be seen that the morphology of the $ZnFe_2O_4$ is particle shape and the particle size is uniform with an average diameter of 20 nm, and due

to its strong magnetism, some $ZnFe_2O_4$ particles agglomerated. In Fig. 6a, some $ZnFe_2O_4$ particles evenly covered on the MoS_2 nanosheets. The results of EDX measurement further confirm the coexistence of Zn, Fe, O, S, and Mo elements in the $MoS_2/ZnFe_2O_4$ photocatalysts (Fig. 6b). The elemental mapping of the $MoS_2/ZnFe_2O_4$ photocatalysts is shown in Fig. 7, which indicated the uniform distribution of elements in the $MoS_2/ZnFe_2O_4$ photocatalysts.

The fine microstructure of the photocatalysts were observed by TEM. Figure 8 exhibits the TEM images of the MoS_2, $ZnFe_2O_4$, and $MoS_2/ZnFe_2O_4$ photocatalysts. In Fig. 8a, the results show that $ZnFe_2O_4$ particles are spherical with an average diameter of 20 nm. In Fig. 8b, it can be seen that MoS_2 is a flower-shaped structure composed of nanosheets. $ZnFe_2O_4$ were deposited on MoS_2 nanosheets and heterogeneous structures were formed between $ZnFe_2O_4$ and MoS_2. Therefore, the light absorption ability of the photocatalysts were improved because of the introduction of nanosheets structure of MoS_2 and the photo-generated electrons by the $ZnFe_2O_4$ in the photocatalytic process can be moved to the MoS_2 nanosheets, consequently, reducing the recombination of photo-generated carriers.

Figure 9 shows the magnetic hysteresis loop of $ZnFe_2O_4$ and $MoS_2/ZnFe_2O_4$ photocatalysts. The magnetization curves of the two photocatalysts are symmetrical, and no hysteresis is observed at the origin, indicating that the photocatalysts have superparamagnetism. The saturation magnetization (M_s) values of two photocatalysts were 11.48 and 4.05 emu g^{-1}, respectively. Although the M_s value was relatively low, the $MoS_2/ZnFe_2O_4$ photocatalysts could effectively realize magnetic separation and recovery revealed by the inset photograph of Fig. 8. Under the external magnetic field, the $MoS_2/ZnFe_2O_4$ photocatalysts were rapidly attracted to the wall of the vial to get a transparent solution, to reduce the loss of photocatalysts, and improve the recovery efficiency.
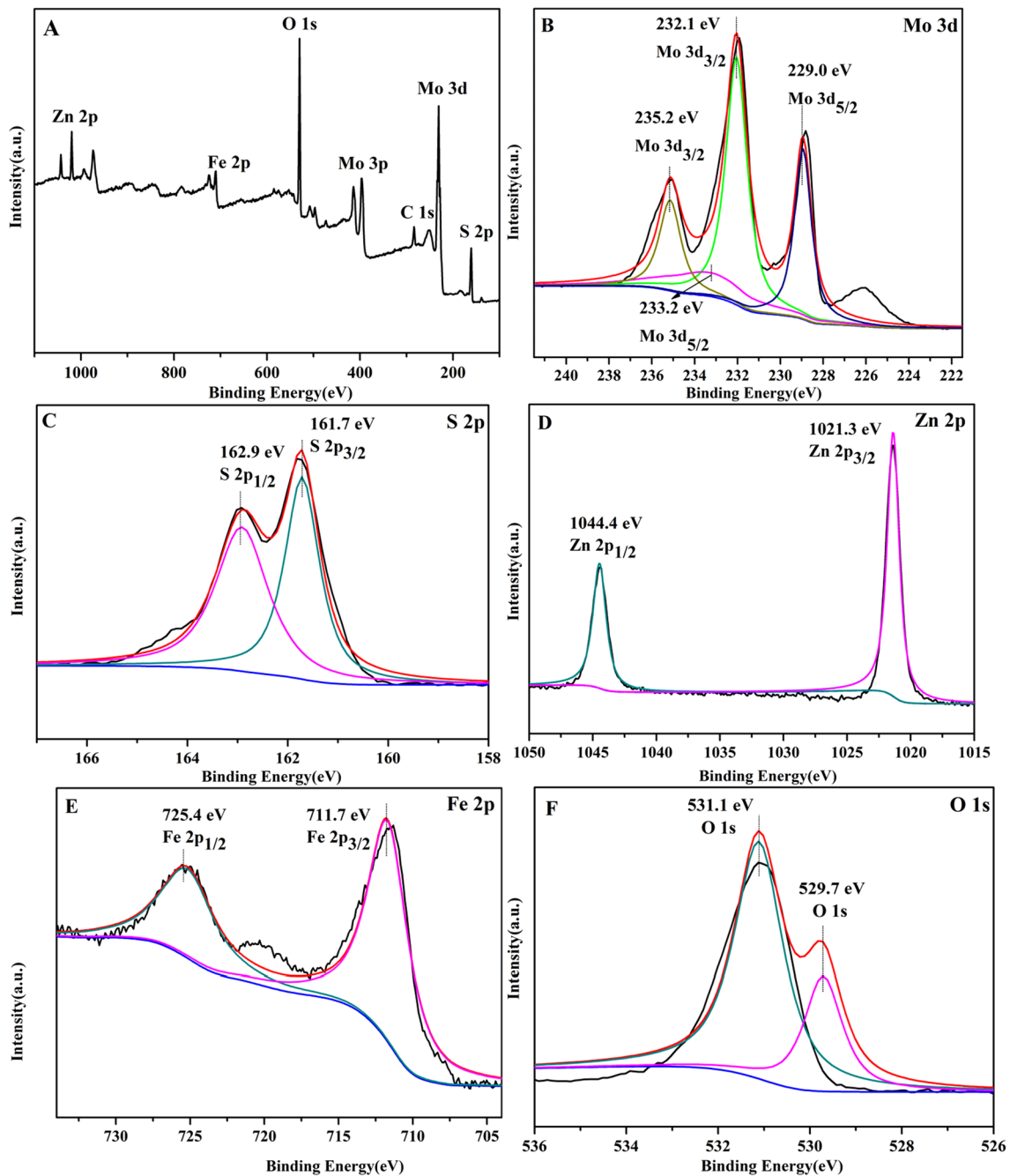
Fig. 4 XPS spectra of the $MoS_2/ZnFe_2O_4$ 25% photocatalysts: **a** XPS survey, **b** Mo 3d, **c** S 1s, **d** Zn 2p, **e** Fe 2p, and **f** O 1s

To reveal the capture, migration, and transfer characteristics of electron–hole pairs, PL emission measurement was used to record the PL spectra of the photocatalysts [22]. Figure 10 displays the PL spectra of the MoS_2, $ZnFe_2O_4$, and $MoS_2/ZnFe_2O_4$ photocatalysts. The results that MoS_2 and $ZnFe_2O_4$ showed very potent photoluminescence emissions centered at 470 nm, the photoluminescence have been quenched remarkably on $MoS_2/ZnFe_2O_4$ photocatalysts, manifesting that the effective photo-generated carriers separation happened, which reveals that the recombination of photo-generated carriers is significantly suppressed, resulting in the increase of highly active species for TC degradation.

Fig. 5 SEM images of the $ZnFe_2O_4$ and MoS_2
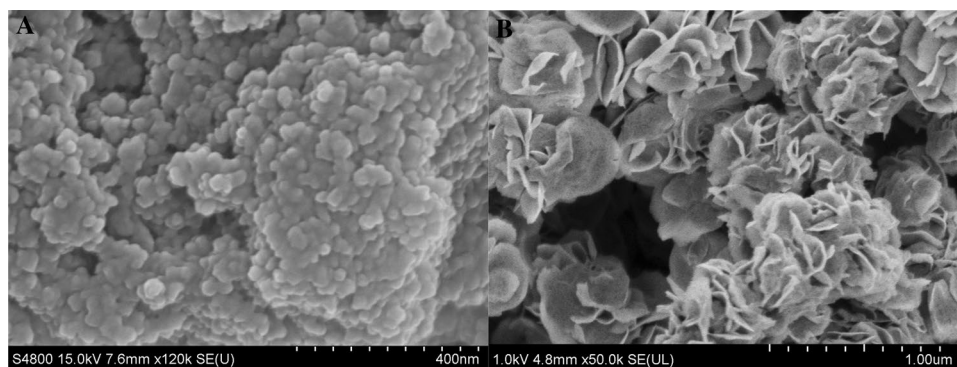
Fig. 6 SEM image and EDS spectra of the $MoS_2/ZnFe_2O_4$ 25% photocatalysts
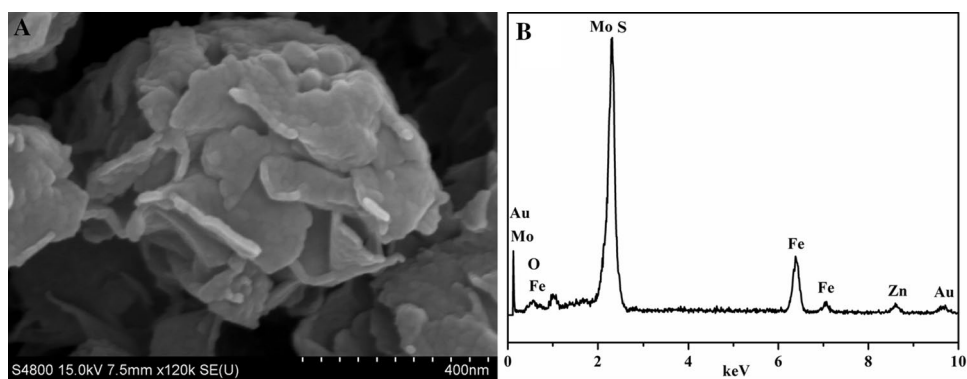
The photocurrent intensity for $MoS_2/ZnFe_2O_4$ 25% photocatalysts is nearly two times and eight times as high as those of $ZnFe_2O_4$ and MoS_2 (Fig. 11a); the result shows that the separation efficiency of electron–hole pairs in $MoS_2/ZnFe_2O_4$ 25% photocatalysts is higher. Therefore, the photocurrent response further proves that heterostructures can improve the separation efficiency of the photo-generated carriers. At the same time, the EIS test was also used to study the process of the charge transfer resistance (Fig. 11b). The values of the radius of the Nyquist circle are consistent with charge transfer resistance [3]. In terms of arc radius, the $MoS_2/ZnFe_2O_4$ 25% photocatalysts show a considerably smaller radius than MoS_2 and $ZnFe_2O_4$. These results coherently demonstrate that $MoS_2/ZnFe_2O_4$ photocatalysts have better photoelectric properties which could improve the separation of the photo-generated carriers in the degradation process.

3.2 Photocatalytic performance

The study evaluated the photocatalytic activity of the photocatalysts by TC photodegradation. Figure 12 shows the photocatalytic performance of different photocatalysts. Through the blank experiment, TC concentration remained stable for 180 min, demonstrating that the photolysis of TC

was neglected without photocatalyst use. The photocatalytic degradation efficiency of TC was low when single MoS_2 and $ZnFe_2O_4$ photocatalysts were used. The photocatalytic activity of $MoS_2/ZnFe_2O_4$ photocatalysts is much higher than MoS_2 and $ZnFe_2O_4$ photocatalysts. $MoS_2/ZnFe_2O_4$-25% photocatalysts show the highest photocatalytic activity with degradation rate of 95%, and the result is consistent with the UV–vis DRS of $MoS_2/ZnFe_2O_4$-25% photocatalysts, which has the highest light absorption capacity.

3.3 Active species capture experiments

The main active species were studied through the active species capturing experiments in the photocatalytic process. For the sake of further study of the photocatalytic mechanism, it is necessary to define which active species play a significant role in the photodegradation process of TC. Scavengers of superoxide radicals ($\cdot O_2^-$), photoexcited holes (h^+), and hydroxyl radicals ($\cdot OH$) were N_2, disodium ethylenediaminetetraacetate (Na_2-EDTA), and tertbutyl alcohol (tBuOH), respectively [31–33]. As shown in Fig. 13, the photocatalytic activity of the $MoS_2/ZnFe_2O_4$ photocatalysts decreased when N_2 was used, suggesting $\cdot O_2^-$ were the main active species in the photocatalytic process. When EDTA and tBuOH were used, the photocatalytic activity of the $MoS_2/$

Fig. 7 The element mapping images of the MoS_2/$ZnFe_2O_4$ 25% photocatalysts: **a** Layered image, **b** O, **c** S, **d** Fe, **e** Zn, **and f** Mo

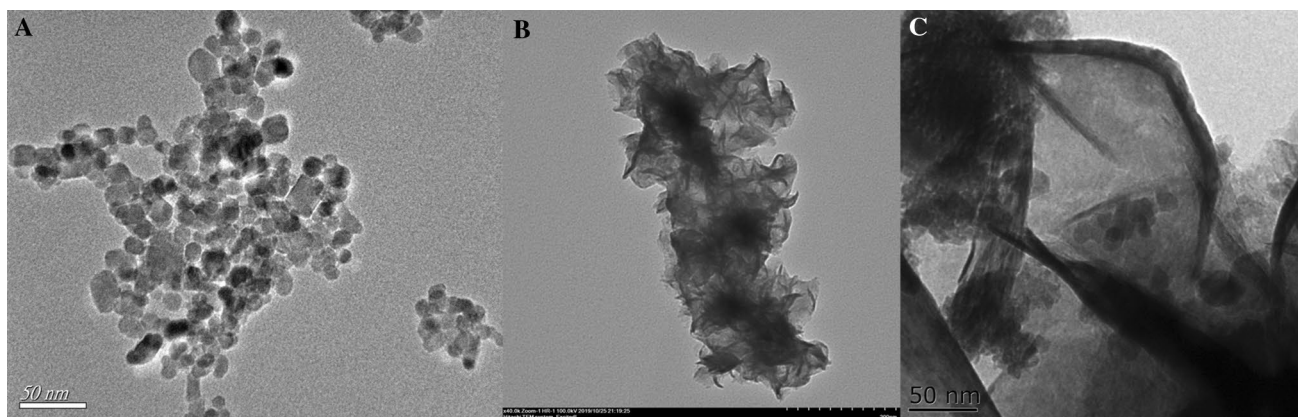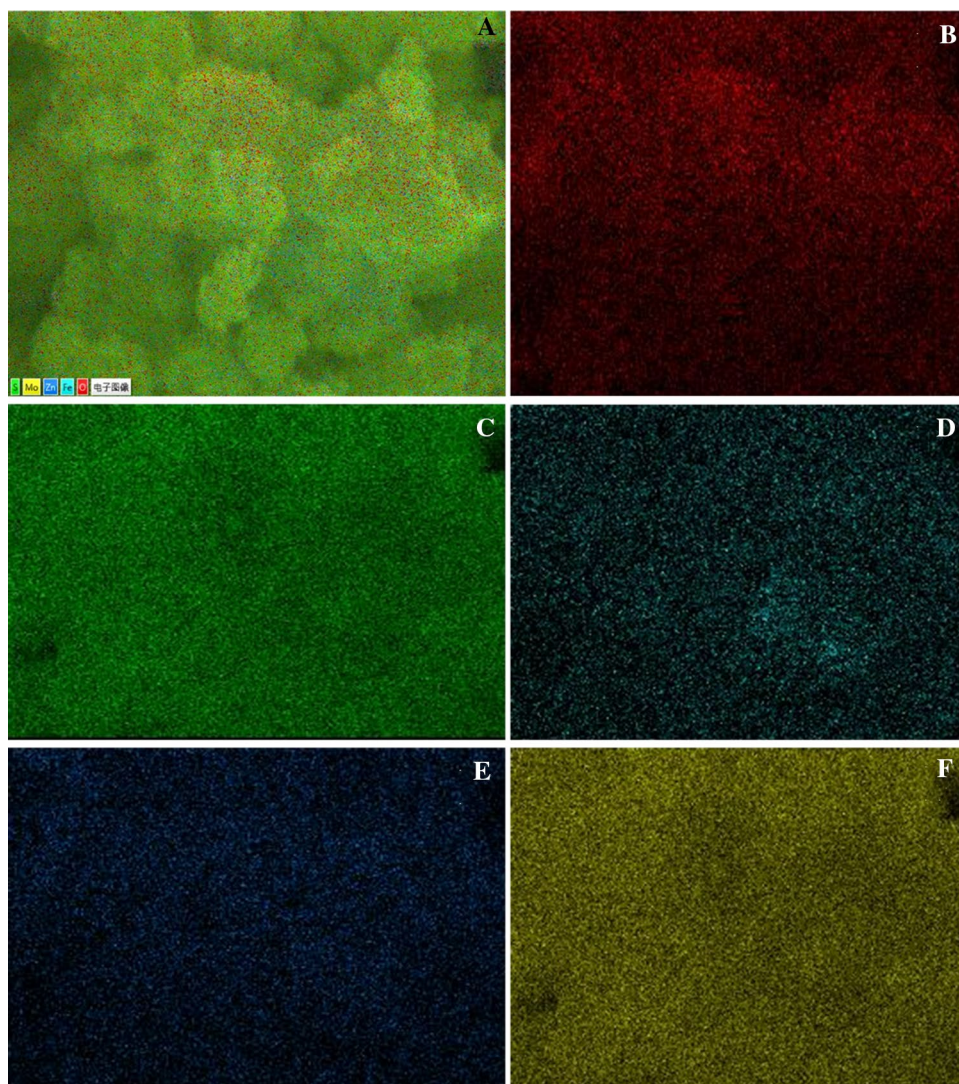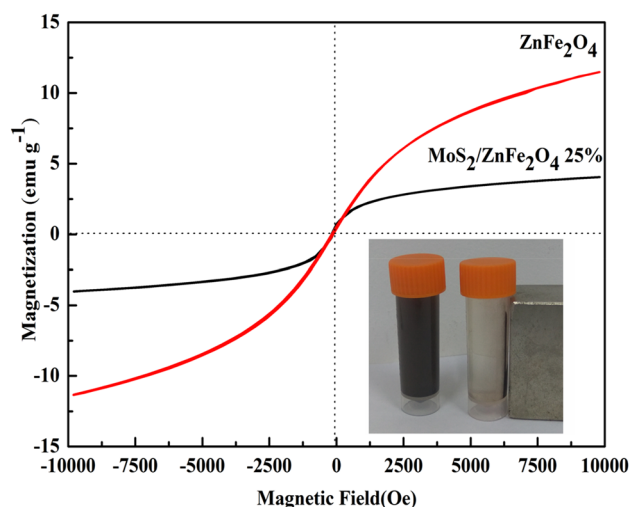**Fig. 8** TEM images of the $ZnFe_2O_4$, MoS_2, and MoS_2/$ZnFe_2O_4$ 25% photocatalysts

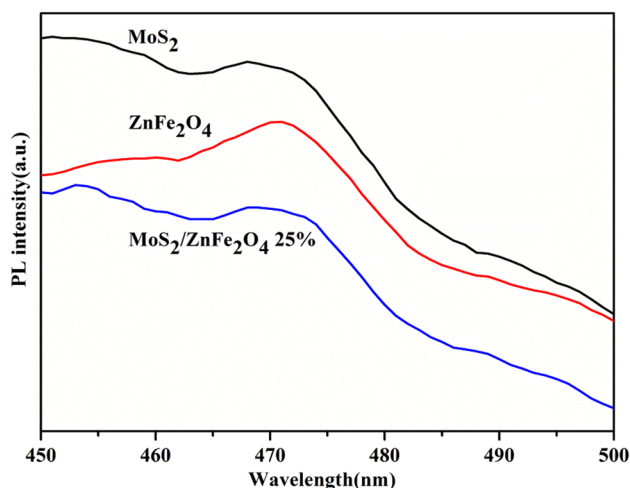**Fig. 9** Magnetic hysteresis loop of the $ZnFe_2O_4$ and $MoS_2/ZnFe_2O_4$ 25% photocatalysts

Fig. 10 PL spectra of the $ZnFe_2O_4$, MoS_2 and $MoS_2/ZnFe_2O_4$ 25% photocatalysts

$ZnFe_2O_4$ photocatalysts decreased slightly, which showed that ·OH and h+ played a smaller role in TC photodegradation. Also, the active species were studied by ESR in the photodegradation process. As can be seen from Fig. 14, ESR signals are weak in the dark, however, it deserves to be mentioned that the six characteristic peaks of $·O_2^-$ can be seen in Fig. 14a, which reveals that the $·O_2^-$ can be generated in the photodegradation process of TC. The characteristic signals of DMPO-·OH have been observed under visible light irradiation (Fig. 14b), indicating that the ·OH

cannot be generated in $MoS_2/ZnFe_2O_4$ photocatalysts in the photodegradation process. In a word, the ESR results are consistent with the capture experiment of active species and the $·O_2^-$ and h+ exist in photodegradation system of $MoS_2/ZnFe_2O_4$ photocatalysts.

3.4 Cycle experiments

Stability is a crucial problem to be considered for practical applications. Figure 15 displays the four-cycle experiment of TC photodegradation with $MoS_2/ZnFe_2O_4$ 25% photocatalysts under the same experimental conditions. The photocatalytic activity has no apparent decrease, showing that $MoS_2/ZnFe_2O_4$ photocatalysts have better photodegradation stability. Figure 16 displays XRD images, SEM picture of $MoS_2/ZnFe_2O_4$ photocatalysts after the reaction, diffraction peaks of MoS_2 (JCPDS card No. 37-1492) [25] and spinel-type $ZnFe_2O_4$ (JCPDS card No. 22-1012) [26]., and morphology of $MoS_2/ZnFe_2O_4$ photocatalysts showing no changes, and these results indicate that $MoS_2/ZnFe_2O_4$ photocatalysts have excellent photodegradation stability.

3.5 Reaction mechanism

As illustrated in Fig. 17a, b (XPS valence band), the VB position of MoS_2 and $ZnFe_2O_4$ are 0.55 eV and 0.47 eV, respectively. Thus, the CB of MoS_2 and $ZnFe_2O_4$ are calculated to be −0.70 eV and -1.50 eV, respectively.

The reaction mechanisms of $MoS_2/ZnFe_2O_4$ photocatalysts include the adsorption and photocatalytic degradation process. The adsorption capacity has a bearing on the specific surface area of $MoS_2/ZnFe_2O_4$ photocatalysts, and photocatalytic degradation is considered to be a robust oxidation process of active species. Based on these data, the tentative mechanism of photocatalytic degradation was discussed in Fig. 18.

In the photocatalytic degradation process of $MoS_2/ZnFe_2O_4$ photocatalysts under visible light illumination, because of its response to visible light, MoS_2 and $ZnFe_2O_4$ can effectively capture photons and induce electrons to excite from VB to CB. Due to the strong thermodynamic driving force generated by the energy difference between the CB of MoS_2 (−0.70 eV) and $ZnFe_2O_4$ (−1.50 eV), the photo-generated electrons in the CB of $ZnFe_2O_4$ are easily transferred to the CB of MoS_2 through the heterojunction structure, which effectively inhibit the recombination of electrons and holes in $ZnFe_2O_4$. Because the CB potential of MoS_2 (−0.70 eV) is more negative than the standard redox potential of O_2/O_2^- (−0.046 eV vs NHE), O_2 on the MoS_2 surface obtain an electron on CB of MoS_2 to produce reactive $·O_2^-$ and hence oxidizes TC. The
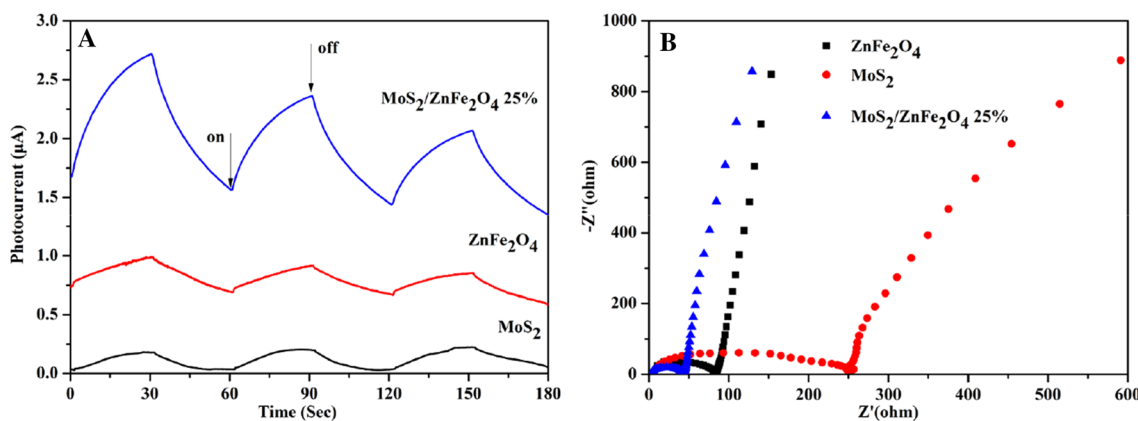
Fig. 11 Transient photocurrent responses spectra (**a**), electrochemical impedance spectra (**b**) of the $ZnFe_2O_4$, MoS_2, and $MoS_2/ZnFe_2O_4$ 25% photocatalysts
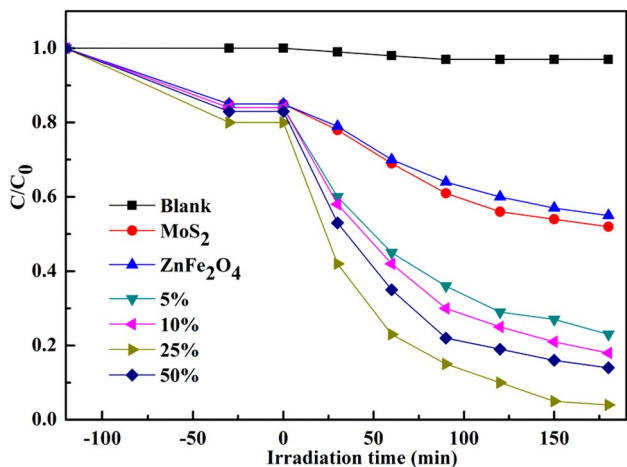

Fig. 12 The degradation rate of $MoS_2/ZnFe_2O_4$ photocatalysts with different composite proportions.
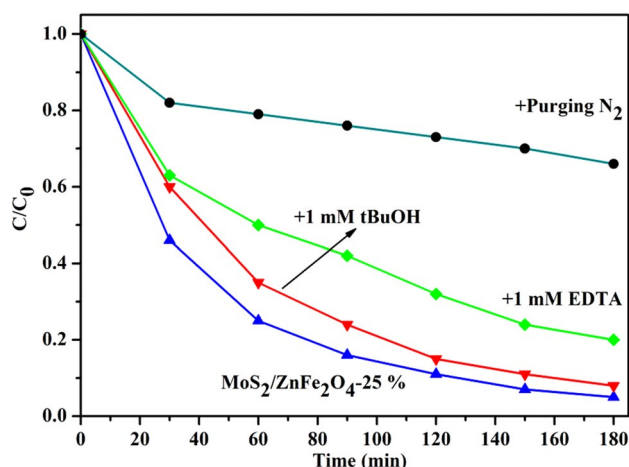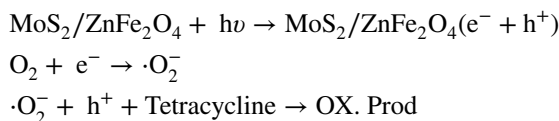

Fig. 13 Plots of photo-generated carriers trapping in the system of photocatalytic degradation of TC over $MoS_2/ZnFe_2O_4$ 25% photocatalysts

photo-generated holes were transferred from VB of MoS_2 to the VB of $ZnFe_2O_4$ because the VB edge potential value of $ZnFe_2O_4$ and MoS_2 is below the standard redox potential of ·OH/OH⁻ (1.99 eV vs NHE); therefore, holes on VB of $ZnFe_2O_4$ cannot react with absorbed H_2O to produce·OH which can directly oxidize TC to produce decomposition products [34]. The close contact interface between MoS_2 and $ZnFe_2O_4$ can effectively inhibit the recombination of the photo-generated electrons and holes, accelerate the photo-generated

electrons transfer speed, and enhance the photocatalytic performance of the photocatalysts.
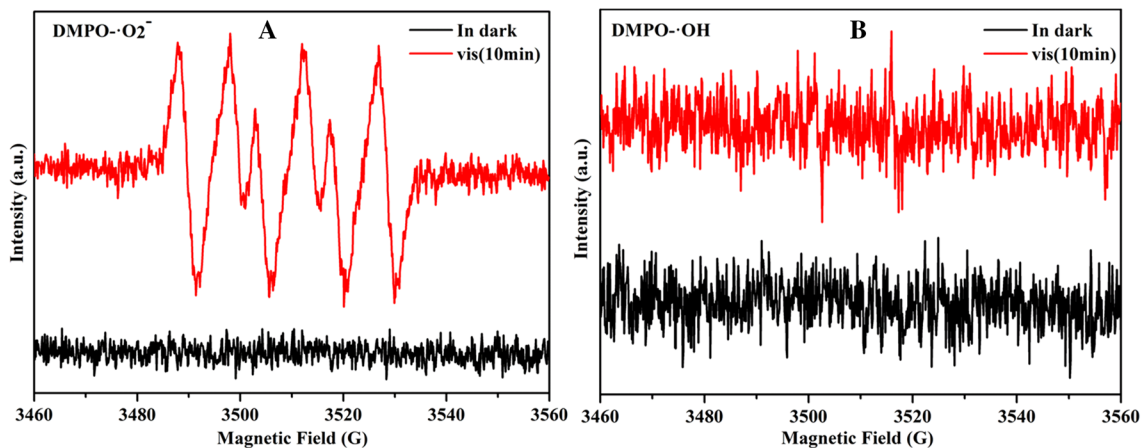
$$MoS_2/ZnFe_2O_4 + h\nu \rightarrow MoS_2/ZnFe_2O_4(e^- + h^+)$$

$$O_2 + e^- \rightarrow \cdot O_2^-$$

$$\cdot O_2^- + h^+ + \text{Tetracycline} \rightarrow \text{OX. Prod}$$

Fig. 14 ESR spectra of DMPO-·OH (**a**) and DMPO-·O_2^- (**b**) for $MoS_2/ZnFe_2O_4$ 25% photocatalysts
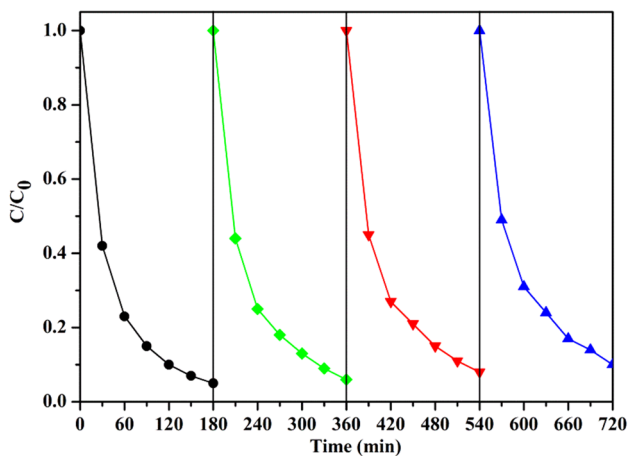

Fig. 15 The figure of four reaction cycles for photodegradation of TC under visible light irrigation with $MoS_2/ZnFe_2O_4$ 25% photocatalysts

4 Conclusion

The study selected a simple hydrothermal method to synthesize the $MoS_2/ZnFe_2O_4$ photocatalysts. The physical and chemical properties of the photocatalysts were characterized by various instruments. The photocatalysts have good visible light response ability and magnetic separation recovery capacity, exhibiting higher photocatalytic performance in the degradation of TC. The $MoS_2/ZnFe_2O_4$ photocatalysts could be reused four times with no significant decrease in the photocatalytic activity. The reason for the high photocatalytic activity of $MoS_2/ZnFe_2O_4$ photocatalysts is due to the introduction of nanosheets structure of MoS_2 and the heterostructures formed by $ZnFe_2O_4$ and MoS_2. Active species capturing experiments reveal that ·O_2^- was the main active species for the photodegradation of TC.
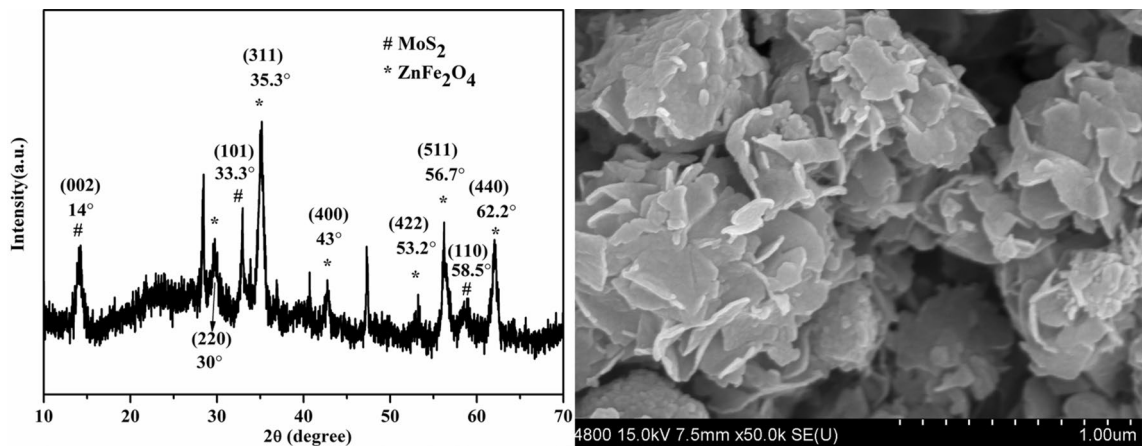

Fig. 16 XRD pattern and SEM image of $MoS_2/ZnFe_2O_4$ 25% photocatalysts after the reaction
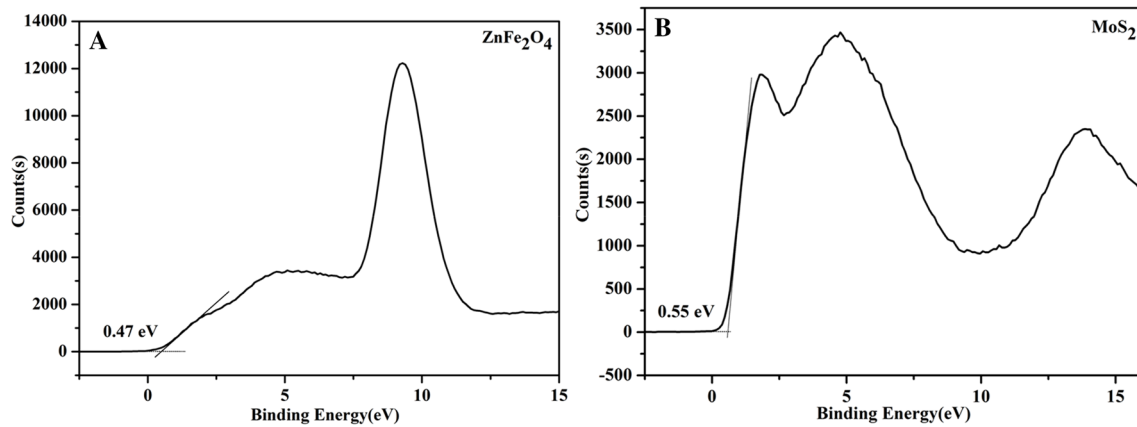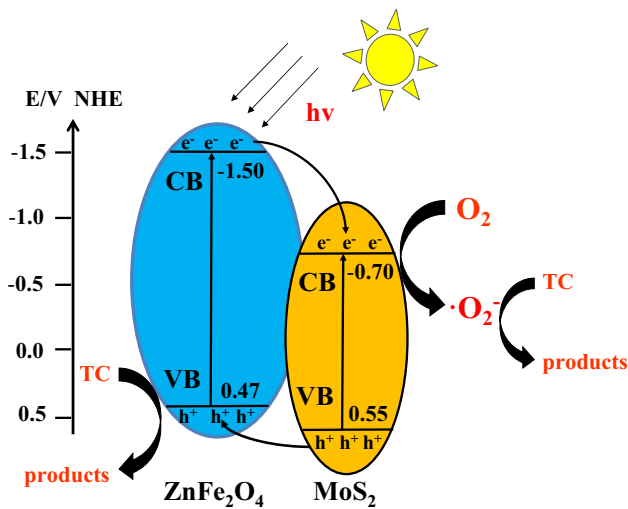
Fig. 17 XPS valence band spectra of $ZnFe_2O_4$ (**a**) and MoS_2 (**b**)

Fig. 18 The mechanism of the photodegradation process on the $MoS_2/ZnFe_2O_4$ photocatalysts

Compliance with ethical standards

Conflicts of interest The authors declare no conflict of interest.

References

1. W. Ma, L. Chen, Y. Zhu et al., Facile synthesis of the magnetic BiOCl/ZnFe₂O₄ heterostructures with enhanced photocatalytic activity under visible-light irradiation. Colloid Surf. A. **508**, 135–141 (2016)
2. X. Ma, C. Dai, L. Yu et al., Energy transfer in plasmonic photocatalytic composites. Light-Sci. Appl. **5**, 16017–16030 (2017)
3. Z. Zhu, X. Tang, T. Wang et al., Insight into the effect of Co-doped to the photocatalytic performance and electronic structure of g-C₃N₄ by first principle. Appl. Catal. B **241**, 319–328 (2019)
4. F. Pincella, K. Isozaki, K. Miki et al., A visible light-driven plasmonic photocatalyst. Light-Sci. Appl. **3**, 133–139 (2014)
5. T. Yatsui, T. Tsuboi, M. Yamaguchi et al., Optically controlled magnetic-field etching on the nano-scale. Light-Sci. Appl. **5**, 16054–16061 (2016)
6. A. Kudo, Y. Miseki, Heterogeneous photocatalyst materials for water splitting. Chem. Soc. Rev. **38**, 253–278 (2009)
7. X. Chen, S. Shen, L. Guo et al., Semiconductor-based photocatalytic hydrogen generation. Chem. Rev. **110**, 6503–6570 (2010)
8. S. Oros-Ruiz, R. Zanella, S. Collins et al., Photocatalytic hydrogen production by Au-MₓOᵧ (M=Ag, Cu, Ni) catalysts supported on TiO₂. Catal. Commun. **47**, 1–6 (2014)
9. F. Wang, Y. Chen, R. Zhu et al., Novel synthesis of magnetic porous C/ZnFe₂O₄ photocatalyst with enhanced activity under visible light based on the Fenton-like reaction. Dalton Trans. **46**, 11306–11317 (2017)
10. N. Khadgi, Y. Li, A.R. Upreti et al., Enhanced photocatalytic degradation of 17α-Ethinylestradiol exhibited by multifunctional ZnFe₂O₄-Ag/rGO nanocomposite under visible light. Photochem. Photobiol. **92**, 238–246 (2016)
11. L. Chen, W. Ma, J. Dai et al., Facile synthesis of highly efficient graphitic-C₃N₄/ZnFe₂O₄ heterostructures enhanced visible-light photocatalysis for spiramycin degradation. Photochem. Photobiol. **328**, 24–32 (2016)
12. W. Ma, L. Chen, J. Dai et al., Magnetic Co₀.₅Zn₀.₅Fe₂O₄ nanoparticle-modified polymeric g-C₃N₄ sheets with enhanced photocatalytic performance for chloromycetin degradation. RSC. Adv. **6**, 48875–48883 (2016)
13. X. Chen, Y. Dai, J. Guo et al., Novel magnetically separable reduced graphene oxide (RGO)/ZnFe₂O₄/Ag₃PO₄ nanocomposites for enhanced photocatalytic performance toward 2, 4-dichlorophenol under visible light. Ind. Eng. Chem. Res. **55**, 568–578 (2016)

14. K. Natarajan, P. Singh, H.C. Bajaj et al., Facile synthesis of TiO_2/$ZnFe_2O_4$ nanocomposite by sol-gel auto combustion method for superior visible light photocatalytic efficiency. Korean J. Chem. Eng. **33**, 1788–1798 (2016)

15. Q. Gu, H. Sun, Z. Xie et al., MoS_2-coated microspheres of self-sensitized carbon nitride for efficient photocatalytic hydrogen generation under visible light irradiation. Appl. Surf. Sci. **396**, 1808–1815 (2017)

16. S. Ma, J. Xie, J. Wen et al., Constructing 2D layered hybrid CdS nanosheets/MoS_2 heterojunctions for enhanced visible-light photocatalytic H_2 generation. Appl. Surf. Sci. **391**, 580–591 (2017)

17. B. Han, S. Liu, N. Zhang et al., One-dimensional CdS@MoS_2 core-shell nanowires for boosted photocatalytic hydrogen evolution under visible light. Appl. Catal. B **202**, 298–304 (2017)

18. S. Zang, G. Zhang, Z. Lan et al., Enhancement of photocatalytic H_2 evolution on pyrene-based polymer promoted by MoS_2 and visible light. Appl. Catal. B **251**, 102–111 (2019)

19. M. Hao, X. Deng, L. Xu et al., Noble metal Free MoS_2/$ZnIn_2S_4$ nanocomposite for acceptorless photocatalytic semi-dehydrogenation of 1, 2, 3, 4-tetrahydroisoquinoline to produce 3, 4-dihydroisoquinoline. Appl. Catal. B **252**, 18–23 (2019)

20. W. Zhang, X. Xiao, Y. Li et al., Liquid-exfoliation of layered MoS_2 for enhancing photocatalytic activity of TiO_2/g-C_3N_4 photocatalyst and DFT study. Appl. Surf. Sci. **389**, 496–506 (2016)

21. J. Li, E. Liu, Y. Ma et al., Synthesis of MoS_2/g-C_3N_4 nanosheets as 2D heterojunction photocatalysts with enhanced visible light activity. Appl. Surf. Sci. **364**, 694–702 (2016)

22. A. Wu, C. Tian, Y. Jiao et al., Sequential two-step hydrothermal growth of MoS_2/CdS core-shell heterojunctions for efficient visible light-driven photocatalytic H_2 evolution. Appl. Catal. B **203**, 955–963 (2017)

23. R.A. Senthil, S. Osman, J. Pan et al., A facile hydrothermal synthesis of visible-light responsive $BiFeWO_6$/MoS_2 composite as superior photocatalyst for degradation of organic pollutants. Ceram. Int. **45**, 18683–18690 (2019)

24. M. Xu, Z. Wei, J. Liu et al., One-pot synthesized visible-light-responsive MoS_2@CdS nanosheets-on-nanospheres for hydrogen evolution from the antibiotic wastewater: Waste to energy insight. Int. J. Hydrogen Energy **44**, 21577–21587 (2019)

25. P. Wang, P. Shi, Y. Hong et al., Facile deposition of Ag_3PO_4 on graphene-like MoS_2 nanosheets for highly efficient photocatalysis. Mater. Res. Bull. **62**, 24–29 (2015)

26. P. Guo, L. Cui, Y. Wang et al., Facile synthesis of $ZnFe_2O_4$ nanoparticles with tunable magnetic and sensing properties. Langmuir **29**, 8997–9003 (2013)

27. G. Padmapriya, A. Manikandan, V. Krishnasamy et al., Spinel $Ni_xZn_{1-x}Fe_2O_4$ ($0.0{\leq}x{\leq}1.0$) nano-photocatalysts: Synthesis, characterization and photocatalytic degradation of methylene blue dye. J. Mol. Struct. **1119**, 39–47 (2016)

28. L. Ye, D. Wang, S. Chen et al., Fabrication and enhanced photoelectrochemical performance of MoS_2/S-Doped g-C_3N_4 heterojunction film. ACS Appl. Mater. Interface **8**, 5280–5289 (2016)

29. Y. Chen, P.D. Tran, P. Boix et al., Silicon decorated with amorphous cobalt molybdenum sulfide catalyst as an efficient photocathode for solar hydrogen generation. ACS Nano **9**, 3829–3836 (2015)

30. Z. Lu, L. Zeng, W. Song et al., In situ synthesis of C-TiO_2/g-C_3N_4 heterojunction nanocomposite as highly visible light active photocatalyst originated from effective interfacial charge transfer. Appl. Catal. B **202**, 488–499 (2017)

31. K. Ding, D. Yu, W. Wang et al., Fabrication of multiple hierarchical heterojunction Ag@AgBr/$BiPO_4$/r-GO with enhanced visible-light-driven photocatalytic activities towards dye degradation. Appl. Surf. Sci. **445**, 39–49 (2018)

32. X. Liu, W. Huang, Y. Lei et al., Effective hydrothermal grafting of Eosin Y onto TiO_2 nanoparticles towards stable photocatalysts for efficient visible-light-driven photocatalytic H_2 evolution. New. J. Chem. **42**, 6631–6635 (2018)

33. H. Anwer, J. Park, Synthesis and characterization of a heterojunction rGO/ZrO_2/Ag_3PO_4 nanocomposite for degradation of organic contaminants. J. Hazard. Mater. **358**, 416–426 (2018)

34. W. Ma, N. Wang, S. Li et al., Synthesis and properties of B-Ni-TiO_2/g-C_3N_4 photocatalyst for degradation of chloramphenicol (CAP) under visible light irradiation. J. Mater. Sci. **29**, 13957–13969 (2018)